

An Advanced *In Situ* Magnetic Resonance Imaging and Ultrasonic Theranostics Nanocomposite Platform: Crossing the Blood–Brain Barrier and Improving the Suppression of Glioblastoma Using Iron–Platinum Nanoparticles in Nanobubbles

Ming-Hsien Chan,[○] William Chen,[○] Chien-Hsiu Li, Chih-Yeu Fang, Yu-Chan Chang, Da-Hua Wei, Ru-Shi Liu,* and Michael Hsiao*



Cite This: *ACS Appl. Mater. Interfaces* 2021, 13, 26759–26769



Read Online

ACCESS |



Metrics & More



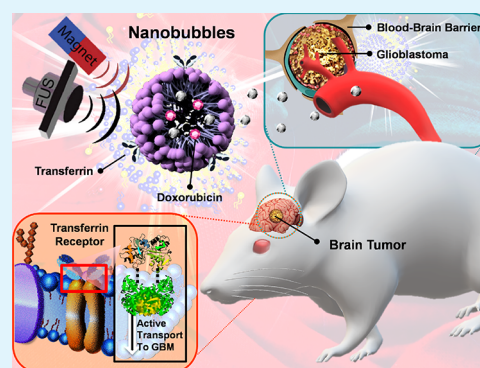
Article Recommendations



Supporting Information

ABSTRACT: Glioblastoma (GBM) is one of the deadliest and most invasive brain cancers/gliomas, and there is currently no established way to treat this disease. The treatment of GBM typically involves intracranial surgery followed by chemotherapy. However, the blood–brain barrier (BBB) impedes the delivery of the chemotherapeutic drug, making the treatment challenging. In this study, we embedded a chemotherapeutic drug and other nanomaterials into a nanobubble (NB), utilized active tracking and other guidance mechanisms to guide the nanocomposite to the tumor site, and then used high-intensity focused ultrasound oscillation to burst the nanobubbles, generating a transient cavitation impact on the BBB and allowing the drug to bypass it and reach the brain. FePt enhances the resolution of T₂-weighted magnetic resonance imaging images and has magnetic properties that help guide the nanocomposite to the tumor location. FePt nanoparticles were loaded into the hydrophobic core of the NBs along with doxorubicin to form a bubble-based drug delivery system (Dox-FePt@NB). The surface of the NBs is modified with a targeting ligand, transferrin (Dox-FePt@NB-Tf), giving the nanocomposite active tracking abilities. The Dox-FePt@NB-Tf developed in the present study represents a potential breakthrough in GBM treatment through improved drug delivery and biological imaging.

KEYWORDS: glioblastoma treatment, blood–brain barrier, nanobubbles, FePt nanoparticles, magnetic resonance imaging



INTRODUCTION

Glioblastoma (GBM) is an aggressive type of brain cancer that has several different treatment methods but remains very difficult to treat.^{1–3} Currently, the primary treatment method includes surgical treatment followed by radiation therapy and then chemotherapy, and the treatment can consist of one or all of these treatments.^{4–6} The treatment of GBM usually involves surgery and radiotherapy to remove the tumor followed by chemotherapy to help clean the remaining cancer cells. This progress is generally the preferred treatment method due to its lower risk of side effects and learning curve in patients. Although chemotherapy is considered for treatment after surgery, it also tends to show inferior effectiveness because the blood–brain barrier (BBB) prevents more than 98% of chemotherapeutic drugs from entering the bloodstream to the brain. The BBB is a semipermeable membrane that is composed mostly of endothelial cells with astrocytes and basement membranes.⁷ These cells create a boundary between the brain and the bloodstream that filters foreign substances, preventing them from entering the brain, and allows only essential nutrients such as oxygen, amino acids, glucose, and

water to pass through. The BBB is crucial in protecting the brain from pathogenic inflammation and infections; however, it also prevents most chemotherapeutic drugs from entering the brain, making intracranial treatment difficult. Other techniques deliver drugs into the brain, but they have drawbacks, including high invasiveness, nonlocal administration, and permanent brain damage.^{8–10} To overcome the BBB, recent studies have shown that high-intensity focused ultrasound (HIFU) oscillations break ultrasonic contrast reagents,^{11–13} such as nanobubbles (NBs), creating temporary cavitation on the BBB and allowing the drugs to pass through and be delivered into the brain locally and noninvasively.^{14–16} When GBM is generated and grown in the brain tissue, it will cause

Received: March 16, 2021

Accepted: May 19, 2021

Published: June 2, 2021



irregularities in the BBB. However, the BBB structure of early generation GBM has not been significantly destroyed, which also makes opening the BBB through ultrasound a means of early drug delivery.^{17–19}

The drug enters the patient's bloodstream, where it is guided by high-precision HIFU guidance until it reaches the brain, where the ultrasonic energy breaks the NBs.^{20–22} NBs allow the drug to be effectively delivered to the brain, where these particles generate small and transient cavitation in the BBB when exposed to ultrasonic oscillation.²³ The cavitation effect is caused by the difference between the internal gas medium and the liquid environment, which, in turn, opens the BBB structure.²⁴ The temporary cavitation in the BBB allows the chemotherapeutic drug, doxorubicin, to reach the brain and treat brain GBM. This treatment allows the monitoring of drug release as well as brain tumors, epilepsy, and other degenerative diseases in the brain.¹⁵ A study has demonstrated that transferrin receptors (TfRs) are overexpressed on brain capillary endothelial cells (a major part of the BBB) and malignant brain tumor cells.²⁵ Therefore, Tf-conjugated nanomedicine delivery systems are used to allow NBs to accumulate around the BBB and GBM. TfRs mediate the Tf-bound iron entry into cells and initiate the formation of an endosome.^{26–28} Ion exchange phenomena similar to this mechanism can be seen commonly in nerve cells, where the upregulation of TfRs facilitates GBM cell proliferation.²⁹ Iron-platinum (FePt) nanoparticles also act as a magnetic resonance imaging (MRI) contrast reagent and are encapsulated in the NB and delivered to the brain to assist in imaging tracking, which is very helpful in the interpretation and diagnosis of GBM.^{30–32} High-resolution imaging diagnoses also increase the accuracy and speed of GBM diagnoses.³³ Current imaging examinations include MRI, computed tomography (CT), electroencephalography (EEG), and cerebrovascular photography.^{34–36} MRI uses magnetic fields to create images of the brain, and it is the most useful form of imaging to diagnose GBM because it allows visualization through the skull and other tissues. MRI also allows the visualization of tumors and blood vessels at the same time, a feature that is important to analyze the spread and metastasis of GBM cells.³⁷ It is also more sensitive than CT, making it better for imaging smaller tumors. Adding additional contrast reagents near the tumor site improves the resolution of the MRI image, which allows us to see the GBM tumor more clearly.^{38–40}

This study is the first to combine nanomaterials (to overcome the BBB with targeted tumor-tracking ability), chemotherapeutics, and MRI contrast agents all in one nanocomposite, Dox-FePt@NB-Tf. Dox-FePt@NB-Tf enters the body via intravenous injection and accumulates in the brain region through magnetic induction. This nanoplatform was labeled with Tf ligands and treated with HIFU at the same time to achieve the active effect of drug accumulation. After ultrasonic treatment, the NB rupture causes a transient cavitation effect that temporarily opens the BBB, where the targeting effect of Tf allows the remaining nanocomposites and Dox to accumulate on GBM for chemotherapy. FePt is transported into the brain alongside Dox in the NB and allows long-term MRI tracking and a high signal-to-noise ratio to improve the resolution of biological images. The nanocomposite developed in this study breaks through the BBB for drug delivery, effectively imaging and tracking the brain tumor, and can target GBM tumor cells to enhance the therapeutic effect of GBM treatment.

EXPERIMENTAL SECTION

Synthesis of FePt NPs. Fe(acac)₃ (0.75 mmol) and Pt(acac)₂ (0.5 mmol) were used as the reaction precursors and were added to the reaction solvent tetraethylene glycol (30 mL) in a 50 mL flask. Argon was introduced into the flask for 30 min for gas replacement. The mixture was heated slowly at 5 °C per minute until the solution reached 200 °C. After holding at 200 °C for an hour, an oleic acid surfactant (1 mL) was added to the mixture. After allowing the mixture to stand at 200 °C for another 30 min, the solution was then heated at 5 °C per minute until it reached 300 °C. During the heating process, the color of the solution was observed to change from blackish red to black, indicating that FePt nanoparticles (NPs) had formed. The mixture was given an hour to reflux, and then ethanol was added. The mixture was then centrifuged at 6000 rpm for 1 h before the procedure for particle purification was carried out. The particles had precipitated due to the increased polarity of the solvent, and the purified FePt NPs were washed five times before being dried, leaving just a black powder that was hydrophilic-phase FePt NPs.

Synthesis of NBs. Three different phospholipids were used to synthesize NBs: DPPC, DPPA, and DSPE-PEG2000-amine. The three phospholipids were combined and dissolved in 4 mL of chloroform. The mixture was given time to evaporate and form a phospholipid film. A surfactant with glycerol (10%) and pluronic F-127 (8 mg) was added to the phospholipid film and placed in a shaking incubator for 1 h at 37 °C. The solution was then sonicated under N₂ and C₃F₈ gases for 2 min to agitate the particles and form the C₃F₈-cored NBs, which were stored at 4 °C.

Synthesis of FePt@NB. The synthesis of FePt@NB was similar to that of the NBs. The same procedures were followed to create the thin phospholipid film. After the film had formed, instead of adding only the surfactant to the phospholipid film, the surfactant was added alongside 0.4 mg of FePt and simultaneously mixed with the thin film on a shaking incubator at 37 °C for 1 h. The solution was then sonicated for 2 min as before to form FePt@NB. The samples were once again stored at 4 °C.

Synthesis of FePt@NB-Tf and Dox Encapsulation (Dox-FePt@NB-Tf). First, an NHS-ester activation process was used for DSPE-PEG2000-amine modifications. EDC (0.4 mg) was added directly to 1 mL of transferrin (Tf). NHS (0.6 mg) was added to the reaction, and the reaction components were mixed well and reacted for 15 min at room temperature. DSPE-PEG2000 was added to the solution containing activated Tf, and the solution was mixed well to allow the reaction to proceed for 2 h at room temperature. The product was the phospholipid Tf-DSPE-PEG2000, the new precursor to synthesize the NBs. For doxorubicin (Dox) encapsulation, 52.5 nM Dox and 0.4 mg of FePt were added to this thin-film suspension before hydration. The suspension was sonicated for 2 min in an ice bath and inflated by octafluoropropane (C₃F₈) in the bubble formation process. The as-prepared NBs were extruded using a 0.45 μm pore syringe filter. Before bubble extrusion, Dox-FePt@NB-Tf was dialyzed using a Cellu-Sep (Dongil Biotech, Seoul, Korea) T1 membrane at 4 °C for 2 h.

Magnetic Vibration and MRI Analysis. A vibrating sample magnetometer (VSM) measures the magnetic field and moment of the material by placing the sample at a fixed frequency in the direction of a certain vertical magnetic field. An electromagnet generated the magnetic field. Two sets of coils were mounted on the two poles of the electromagnet to measure the changes in the magnetic field, and the voltage signal may be induced to obtain a hysteresis curve. The magnetic properties of the FePt@NB nanocomposites were measured using a VSM at normal room temperature with an applied magnetic field of 16,000 to −16,000 Oe. T2-weighted MRI was performed using the multi-slice multi-echo (MSME) method (TR/TE = 8000/8 ms; slice thickness = 1.5 mm) using a 7 T scanner (*in vivo* BRUKER Biospec 7 T 40 cm bore horizontal MRI system; Karlsruhe, Germany). For *in vivo* MRI T2-weighted imaging and the parameter settings for a 7 T magnetic field, we set echo spacing = 8 ms, TE = 15 ms, FOV = 6.5 × 6.5 cm², matrix size = 256 × 256, NEX = 2, and concentration of added FePt@NB = 0.1–1.6 mM.

Evaluating the Expression of TFRC1 in TCGA, Rembrandt, and the Human Protein Atlas Database. The related TFRC1 expression was analyzed from the Gene Expression Profiling Interactive Analysis (GEPIA, <http://gepia.cancer-pku.cn/>) and the Gliovis website (<http://gliovis.bioinfo.cnio.es/>). The GEPIA website is based on the UCSC Xena project (<http://xena.ucsc.edu>) with the standard pipeline from the Cancer Genome Atlas (TCGA) database, including brain tumors. The Gliovis website is included in the Rembrandt microarray database, which contains 874 glioma specimens, including 566 gene expression arrays, 834 copy number arrays, and 13,472 clinical phenotype data points. In this study, we compared the related expression of TFRC1 in brain tumor patients based on the TCGA and Rembrandt datasets. The TFRC1 expression level demonstrates in the Human Protein Atlas (HPA) dataset to compare the difference between a normal brain tissue and GBM by the histochemical staining evaluation (<https://www.proteinatlas.org/ENSG00000072274-TFRC1>).

Cellular Uptake and Localization Analysis. Approximately 20,000 cells/mL SVG p12 or D54MG cells was plated on a well plate slide for 12 h, and 250 $\mu\text{g/mL}$ FePt@NB or FePt@NB-Tf was added to the culture followed by incubation at 37 °C in 5% CO₂ for 12 h. The cells were washed with 10 mM phosphate-buffered saline (PBS; pH 7.4) and fixed in 4% paraformaldehyde to maintain their intrinsic form. The dye DAPI was added for nuclear staining. After 5 min of incubation, the dye was removed and observed using laser scanning confocal microscopy (LSCM). The DAPI-stained nuclei were excited at 408 nm, and the emission image was detected at 450–500 nm. FePt@NB and FePt@NB-Tf were also stained with the labeling dye, DiI, which is excited by 550 nm green light, and its emission was detected as a yellow to orange fluorescence at 565 nm.

In Vivo Phototherapeutic Effect. The Institutional Animal Care and Utilization Committees of Academia Sinica approved all the animal experiments (IACUC no. 16-05-957). The NOD-SCID (NS) mouse experiment was divided into two parts: one part was a subcutaneous tumor injection assessment, and the other part was an orthotopic brain tumor injection evaluation (the detailed MRI information of the mice is mentioned in the [Supporting Information](#)).

Subcutaneous Tumor Injection. The D54MG GBM cancer cell line (5×10^6 cells/100 μL) was injected subcutaneously into the right thigh of the mouse. The control, FePt@NB, Dox-FePt@NB, and Dox-FePt@NB-Tf nanocomposites (100 mg) were intravenously injected into the tumors when the latter had grown to 125 mm³ during the fourth week. The drug administration process used 10 mg/kg samples for the treatment of each mouse via intravenous injection (I.V.).

Orthotopic Brain Tumor Injection. Initially, the head surface of an anesthetized mouse was disinfected with 70% alcohol. The hair on the head was shaved, and a 10–15 mm sagittal incision was made with a sterile scalpel. The optimum number of cells injected (5×10^5 D54MG cells) was resuspended in 3–5 μL of PBS. The syringe was slowly lowered to a depth of 3 mm below the surface of the skull. After the needle entered the brain, the cells were penetrated slowly via an electric pump at a rate of 1 μL per minute for 6–8 min to avoid any backflow. The samples were injected into the mice, as described above. The only difference was the use of a magnet to guide the materials to accumulate in the brain tissue and treatment with ultrasonic energy to break the BBB and send the drug into GBM cells.

Histochemical Staining (Hematoxylin and Eosin Stain) and Inductively Coupled Plasma Mass Spectrometry (ICP-MS). All the tumors were acquired after 10 weeks. The tumor sections were formalin-fixed and paraffin-embedded. Cross sections of the tumor were stained with hematoxylin and eosin (H&E). Each tumor taken from the formalin-fixed, paraffin-embedded tissues was selected using the morphology that is typical for the diagnosis. A Leica ST5010 Autostainer XL (Wetzlar, Germany) was used for H&E staining. Briefly, the sections were dewaxed in a 60 °C oven, deparaffinized in xylene, and rehydrated in graded alcohol. All the stained tumor sections were observed using a Leica Aperio AT2 scanner. For the ICP-MS (X series II, Thermo) analysis, the Fe⁵⁶ element was chosen to confirm the biodistribution and test the DOX-FePt@NB-Tf. The

tissue (5 mg) of each organ (especially the brain tumor) was dissolved in nitric acid at 60 °C overnight. After the tissue dissolved, the buffer was used to dilute the sample solution with a concentration of 1:10000. The diluted sample solution was passed using a Millex-GN filter (0.2 μm , nylon 13 mm) to remove impurities and obtain the analytical sample for ICP-MS.

RESULTS AND DISCUSSION

Characterization of the Basic Physical Structure of FePt@NBs. To characterize the basic physical structure of FePt@NBs, we designed and performed the procedures of the Dox-FePt@NB-Tf nanosystem in the vessel ([Figure 1](#)). The

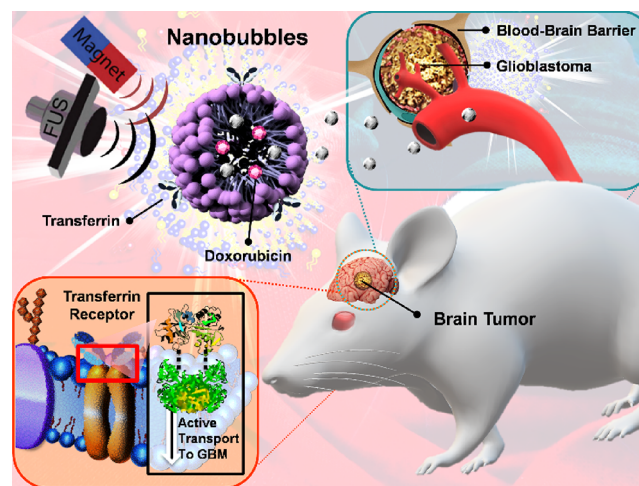


Figure 1. Design of the nanosystem for glioblastoma cell treatment. The targeted system, Dox-FePt@NB-Tf, can be guided using magnetism and ultrasound to treat glioblastoma.

nanosystem comprising Dox and FePt NPs embedded in NB carriers accumulated at the GBM tumors using Tf/TfR targeting. Ultrasonic induction was used to break the surface of the BBB and cause brief cavitation, allowing the Dox drug and FePt NPs from the NBs to pass through the BBB to treat and track (with MRI) the treatment effect of GBMs. [Figure 2a](#) shows the structure of Dox-FePt@NB-Tf, which was used as the magnetic and ultrasonic theranostic guidance platform.

After the FePt NPs were encapsulated in the lipid precursors and functionalized with transferrin, FePt@NB-Tf was analyzed using several different methods. Transmission electron microscopy (TEM) was used to measure the size and *d*-spacing of FePt NPs, which had a diameter of approximately 3–5 nm and a *d*-spacing of 0.3 nm ([Figure S1a,c](#)). To determine the crystal plane of FePt NPs, the TEM image was differentiated by the selected area electron diffraction (SAED) pattern and peaks (111) and (200) were matched in the X-ray diffraction (XRD) pattern ([Figure S1d,e](#)). A scanning transmission electron microscopy energy-dispersive spectrometer was used to confirm that the Fe and Pt elemental ions showed specific alloy distribution and that they had successfully formed FePt NPs ([Figure S1f,i](#)). The characteristics of the NBs were evaluated using TEM, SEM, and confocal microscopy. We synthesized the core–shell structure of Dox encapsulated in NBs using a C₃F₈ hydrophobic core and the three phospholipids DPPC, DPPA, and DSPE-PEG2000-amine as the shell ([Figure S2a,b](#)). The lipid surface of the NBs was doped with a DiI dye, which formed a red fluorescent circle around the lipid layer of NBs when examined by confocal

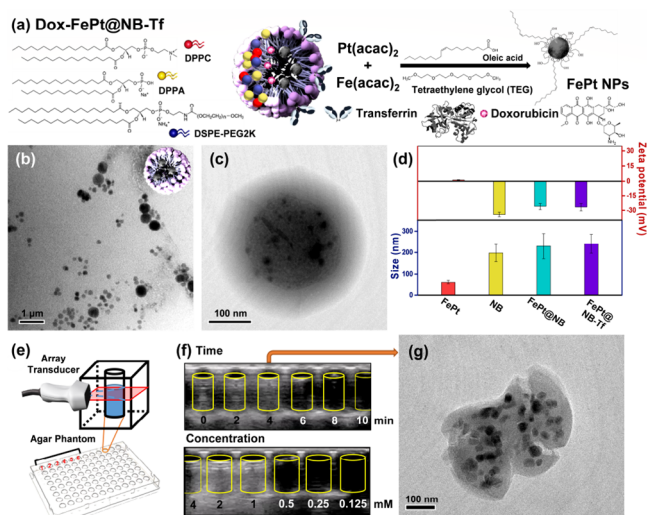


Figure 2. Basic material identification of Dox-FePt@NB-Tf. (a) Schematic diagram of the combination of nanomaterials to form the nanocomposite material Dox-FePt@NB-Tf. (b) TEM (transmission electron microscopy) image of FePt@NBs and (c) zoomed-in image on a single FePt@NB to prove that FePt NPs are embedded in the NB. (d) Zeta potential and DLS test the surface potential and size of various particles. (e) Schematic diagram of the ultrasonic equipment setup that was used to obtain ultrasonic images of each sample in the 96 wells. (f) Ultrasonic images of FePt@NB in a concentration gradient over time when exposed to ultrasound. (g) TEM image of FePt@NB with a fractured NB after ultrasonic treatment for 4 min.

microscopy (Figure S2c). Herein, Figure 2b presents the TEM images of FePt@NB, indicating that uniform singlet NBs were evenly dispersed throughout the copper mesh. A typical liposphere was approximately 200 nm in size. Image enlargement showed that the FePt NPs were encapsulated in the cavity of the NBs (Figure 2c). The size and surface electrical distribution of the nanoparticles were detected using dynamic light scattering (DLS) and the zeta potential (Figure S3a,b). In Figure 2d, the almost uncharged FePt NPs had a particle size of 50 nm. The aggregation of FePt in water produced a significant increase in the hydration radius. After the FePt NPs were embedded in the NBs, they had a particle size of approximately 200–300 nm, which matched the TEM image due to uniform dispersion. Adding FePt NPs to the NBs showed an insignificant effect on their particle size. The NB surface was also negatively charged because it is a lipid layer. Figure 2e shows a schematic diagram of the ultrasonic device. We divided the ultrasonic test group into two groups. The first group was tested immediately after the ultrasonic wave broke the FePt@NB. The concentration of the solution was kept constant at 1 mM, and the FePt@NB sample was processed by the ultrasonic wave for 0, 2, 4, 6, 8, and 10 min. The bubbles began to rupture after about 6 min (Figure 2f), and the ultrasonic signal that was generated by the FePt@NBs was no longer observable after 10 min.

Next, 4, 2, 1, 0.5, 0.25, and 0.125 mM FePt@NB solutions were used for the test, and consecutive TEM images at different time points are shown in Figure S4a,b. The results showed that the ultrasonic contrast agent likely had a concentration sufficient to generate echo information to be detected by the transducer. We also treated 1 mM FePt@NBs with ultrasound for 4 min and observed them by TEM. A TEM

image of a nanobubble broken with ultrasound is shown in Figure 2g.

Magnetic Properties of FePt@NB. FePt has excellent T2-weighted MRI imaging capabilities. As a hard magnetic material, it has ferromagnetism and high magnetocrystalline anisotropy.⁴¹ It has also been applied extensively in biomedical fields. The superparamagnetism of FePt NPs makes them attractive candidates for use as MRI/CT scan agents and as a high-density recording material. An MRI image of FePt and Fe₃O₄ is shown in Figure S5a. Compared with Fe₃O₄, FePt has a higher magnetic out-of-phase constant K_u value and saturation magnetization than other materials.⁴² T2-weighted MRI images using a FePt concentration of at least 0.64 mg/mL showed noticeable quality advantages compared with T2-weighted MRI images without FePt. A significant MRI variation was also achieved in quantifying the T2-weighted values (Figure S5b).

In Figure S5c, which shows the linear regression of $1/T_2$, R^2 is $17.18 \text{ mM}^{-1} \text{ s}^{-1}$, indicating that FePt NPs can reduce the lateral relaxation time and serve as a contrast agent for MRI to reduce the signal strength of magnetic resonance. The saturation magnetization of FePt (Figure S5d) measured using a vibrating sample magnetometer (VSM) was 9.745 emu/g and showed a paramagnetic magnetic behavior. NBs were used as an encapsulation vehicle, and the experimental design using MRI for mouse evaluation is demonstrated in Figure 3a. The measured FePt@NB nanocomposites revealed

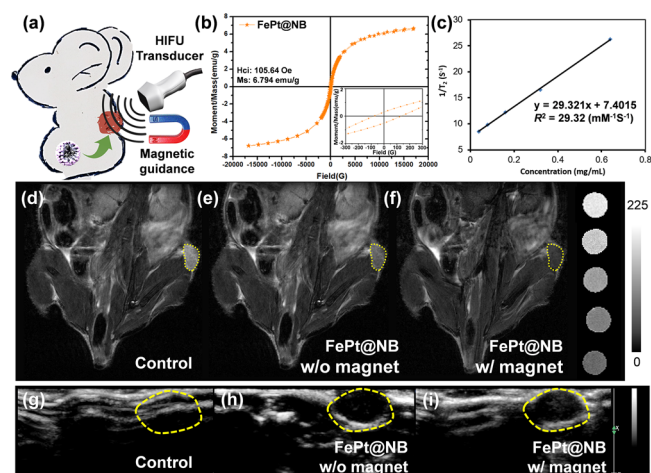


Figure 3. T2-weighted MRI and ultrasonic tumor imaging. (a) Schematic diagram of ultrasonic and magnetic guidance MRI. A magnet guides the FePt@NB to the tumor site. Next, a HIFU transducer creates an ultrasonic wave to break the NB and release FePt. (b) VSM curve of FePt@NB (inset: the enlarged curve between -300 and 300 emu). (c) T2-weighted calibration curve of FePt@NB. (d–f) T2-weighted MRI images of tumor contrast evaluation. The MRI image of the tumor site is the brightest in the control group, and it is darker in the FePt@NB group. In the FePt@NB group with the magnet, the tumor site is even darker than both previous groups. (g–i) The ultrasonic images demonstrate that NBs can be applied for tumor imaging as they darken the tumor region.

an R^2 value of $29.32 \text{ mM}^{-1} \text{ s}^{-1}$ and a saturation magnetization of 6.794 emu/g, indicating that the MRI signals of FePt@NB and FePt NPs are not significantly different (Figure 3b,c). FePt@NB is useful in two different types of image-rendering techniques. The first involves using MRI and ultrasonic image processing simultaneously. For this imaging technique, FePt@

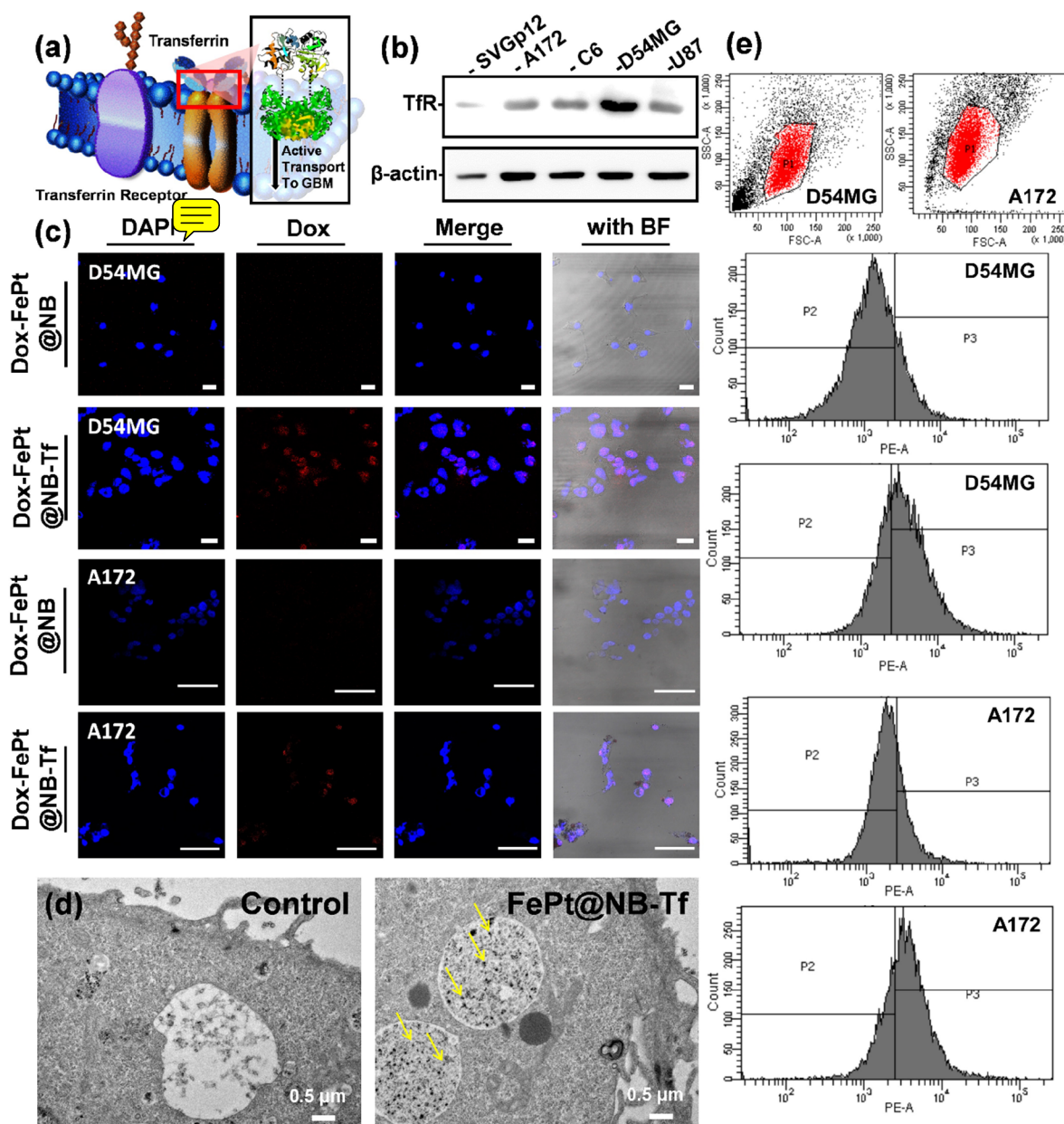


Figure 4. Evaluation of active transferrin targeting. (a) Schematic diagram of Tf attaching to TfR, which actively transports it into GBM. (b) Western blotting results show the amounts of TfR present in different cell types. (c) Confocal images of FePt@NB stained with DAPI and fluorescent Dox in D54MG and A172 cells. Cryo-EM images of D54MG cell slices show different (d) control and FePt@NB groups. The yellow arrows point to the FePt@NB particles in D54MG cells. (e) Flow cytometry plots show the trend of endocytosis with targeting Tf in D54MG and A172 gliomas.

NB makes it easier to distinguish the tumor location and aids analysis by improving the image resolution. Figure 3d,f shows MRI images of mice. D54MG cells were the test cells used in this experiment, and 5×10^6 D54MG cells were implanted under the skin of the right thigh of the mouse. After 3 weeks, FePt@NB was injected intravenously into the mice at doses of 10 mg/kg. MRI was used to observe the tumor shape. After FePt@NB was injected and guided to the tumor site by attraction to a magnet, a clear dark-field contrast was obtained using a 7 T MRI machine and showed that FePt@NB had produced significant changes in the T2-weighted MRI images of the mouse system.³² Moreover, the T2 cortex SNR was used to quantify the subcutaneous groups of control, FePt w/o the magnet, and FePt w/ the magnet and the values are 92, 75, and

63, respectively. Compared with the control group, this can increase the signal of T2 contrast by 32% after being attracted to an external magnetic field. Figure 3g,i shows ultrasound images. In contrast to the control group, the appearance of a tumor edge was obtained immediately after the addition of FePt@NB. After using a magnet to actively guide the NBs to the tumor site, the ultrasonic signal of the bubbles showed that the NBs had accumulated at the tumor site.

Targeting Ability of Transferrin (Tf) for Glioma Cell Lines. The expression of TFRC1 (transferrin receptor 1, TfR) can be evaluated in the TCGA and Rembrandt (Repository of Molecular Brain Neoplasia Data) datasets to provide clinical relevance of TfR expression in human glioma samples. In Figure S6a,b, we compared TfR expression of low-grade vs

high-grade glioma as well as a normal brain vs low/high-grade glioma (TCGA datasets). Moreover, we also arranged the GBM data by their grades and observed that the TfR expression in high-grade gliomas is higher than that in low-grade gliomas (Rembrandt datasets). Based on the results of these analyses, we can infer that high-grade GBM has a high expression level of TfR. Moreover, the histochemical staining of primary human GBM samples in the online database Human Protein Atlas (HPA) is available to evaluate TfR protein expression. In Figure S6c, the TFRC antibody was used to stain different patients. Compared with the GBM samples and normal brain staining, no obvious expression of TfR can be detected in the normal brain tissues. In addition, immunostaining results demonstrate that the staining pattern of GBM tissues is membranous, which confirms that TfR indeed has a higher expression in glioma cells than the normal tissues' surroundings. To provide more information about the modified Tf-DSPE-PEG2000, we measured the NMR (Figure S7a) and ICP-MS (Figure S7b) data to confirm that Tf was modified with the DSPE-PEG2000-amine. The ^1H -NMR spectra signals at 3.5–3.8 ppm attributed to the most characteristic peak protons of DSPE-PEG2000-amine, and those at 3.40–3.85 (4 $n\text{H}-(\text{CH}_2\text{CH}_2\text{O})_n-$) ppm were the methylene protons of PEG. The proton peaks of DSPE-PEG2000-amine and Tf were chemically small-shifted due to the steric effect (4.82–4.65 and 3.34–3.2 ppm). The specific peak of Tf was introduced to the modification with DSPE. Since the molecular weight of DSPE-PEG2000-amine is not consistent and depends on the modified PEG, DSPE-PEG2000-amine showed an interval distribution at $M_w = 2700$ in the mass spectrum. The addition of Tf molecules combined with DSPE-PEG2000-amine could be observed as a significant shift in mass ($\Delta\text{MS} = 457.285$).

Arising from the starting N-terminal amino acid sequence of Tf, which is "VPDK" and could be digested by trypsin during sample processing, it was confirmed that Tf is indeed compatible with DSPE-PEG2000-amine conjugation. We confirmed the transferrin's (Tf) ability to facilitate receptor-mediated transcytosis in several intracranial orthotopic mouse models of glioma cells (Figure 4a): SVG p12 (the human fetal brain cell line) and A172, C6, D54MG, and U87MG (glioma cell lines).⁴³ Western blot analysis demonstrated that the expression of Tf receptors in D54MG cells was significantly greater than that of SVG p12 cells and relatively greater than that of any of the other tumors observed (Figure 4b). To be a clear comparison, we chose A172 cells as the low TfR expression group to compare the expression levels of TfR in different cells that will affect the cellular uptake ability of FePt@NB-Tf. Next, we compared the LSCM images of D54MG and A172 cells incubated with Dox-FePt@NB and D54MG cells incubated with Dox-FePt@NB-Tf. The D54MG cells incubated with Dox-FePt@NB-Tf showed stronger fluorescence signals coming from the region of the cells than A172 cells, indicating that Tf had successfully guided Dox into the nucleus of the tumor cells (Figure 4c). This intracellular uptake was then quantified by cryo-EM, which revealed the distribution of the D54MG cells incubated with Dox-FePt@NB and Dox-FePt@NB-Tf. More materials appeared to enter the cells after the modification of Tf onto the surface of the NBs. The distribution of FePt@NB in D54MG cells using Tf as a tumor-targeting probe was observed in the endosome and showed that more materials had entered the cells (Figure 4d). These results suggested that functionalizing FePt@NB with Tf

is required for the efficient cellular uptake of FePt@NB into the D54MG glioma cells. The quantifying endocytosis efficiency of Dox-FePt@NB-Tf between D54MG and A172 can also be demonstrated by flow cytometry. It is worth noting that, since the Dox-FePt@NB-Tf is facilitating the uptake by D54MG, the amount of cell fragments is more than A172 (the first quadrant in Figure 4e). The results also indicated that the nanocomposites are accumulated in D54MG cells and cause death.

Analysis of Drug Release in the Brain and *In Vitro* Cytotoxicity.

Drug release and cytotoxicity tests were conducted to prove that the drugs could be successfully released into the brain safely. Dox-FePt@NB was applied onto an osmotic membrane where an ultrasound transducer was used to stimulate it and cause the drug to be released into the solution environment outside of the membrane.⁴⁴ Figure S8a confirms that, after Dox-FePt@NB had been subjected to 7 MHz ultrasonic treatment for 5 min, the NBs broke, causing Dox to be released and transmitted into the solution through UV-vis for 5 min. To confirm that the broken NBs were caused by ultrasonic damage, we confirmed that the encapsulated nanoparticles were released in a very short time. In Figure S9a, ultrasonic treatment was performed at 20, 100, and 180 s. After each treatment, a stronger Dox absorption peak was obtained, confirming that the drug was released because of the bubble burst.⁴⁵ Additionally, to evaluate the amount of DOX, we use the UV-vis spectrometer to measure the spectrum of DOX (Figure S9b). The encapsulation efficiency and loading capacity of Dox in the NBs had been quantified with a specific absorption wavelength of DOX at 480 nm. Before performing the *in vivo* tests, we evaluated the ultrasonic effect and therapeutic efficacy of the Dox-FePt@NB-Tf nanosystem using the cell viability assay. To compare the impact of ultrasound on the material, we designed another set of experiments using transwells to confirm the therapeutic effect of the drug. First, we placed the sample in a transwell with a pore size of 0.4 μm (compared with the drug DOX, the NB should not easily pass through). The groups were divided into samples with or without ultrasound, and then the transwells were placed into the 24-well plate of the cultured cells. The cell compatibility test was carried out after 24 h of incubation. In Figure S8b, the drug transports through the pore and causes cell death.

However, if only ultrasonic processing is used, then biosafety tests of the different ultrasonic treatment groups confirmed that the energy waves did not cause cell damage (Figure S8c). Dox-FePt@NB and Dox-FePt@NB-Tf effectively entered the SVG p12 cells after 4 h of incubation but did not produce any obvious effects on cell viability after 24 h, even at a concentration of 250 mg/mL , indicating that the nanomaterials had excellent biocompatibility (Figure S9c). Next, we compared Dox-FePt@NB and Dox-FePt@NB-Tf using glioma cells. The three materials were compared in D54MG cells, and the increased concentrations of Dox-FePt@NB and Dox-FePt@NB-Tf resulted in decreased cell viability. The Dox-FePt@NB-Tf nanosystem killed half of the gliomas at 83 mg/mL and killed 70% of the gliomas at 250 mg/mL because of the targeting effect of transferrin (Figure S9d).

Evaluation of the Therapeutic Efficacies of FePt@NB, Dox-FePt@NB, and Dox-FePt@NB-Tf. Evaluation of the therapeutic efficiencies of FePt@NB, Dox-FePt@NB, and Dox-FePt@NB-Tf was performed to prove that Dox-FePt@NB-Tf had a superior ability to deliver the drug to the glioma

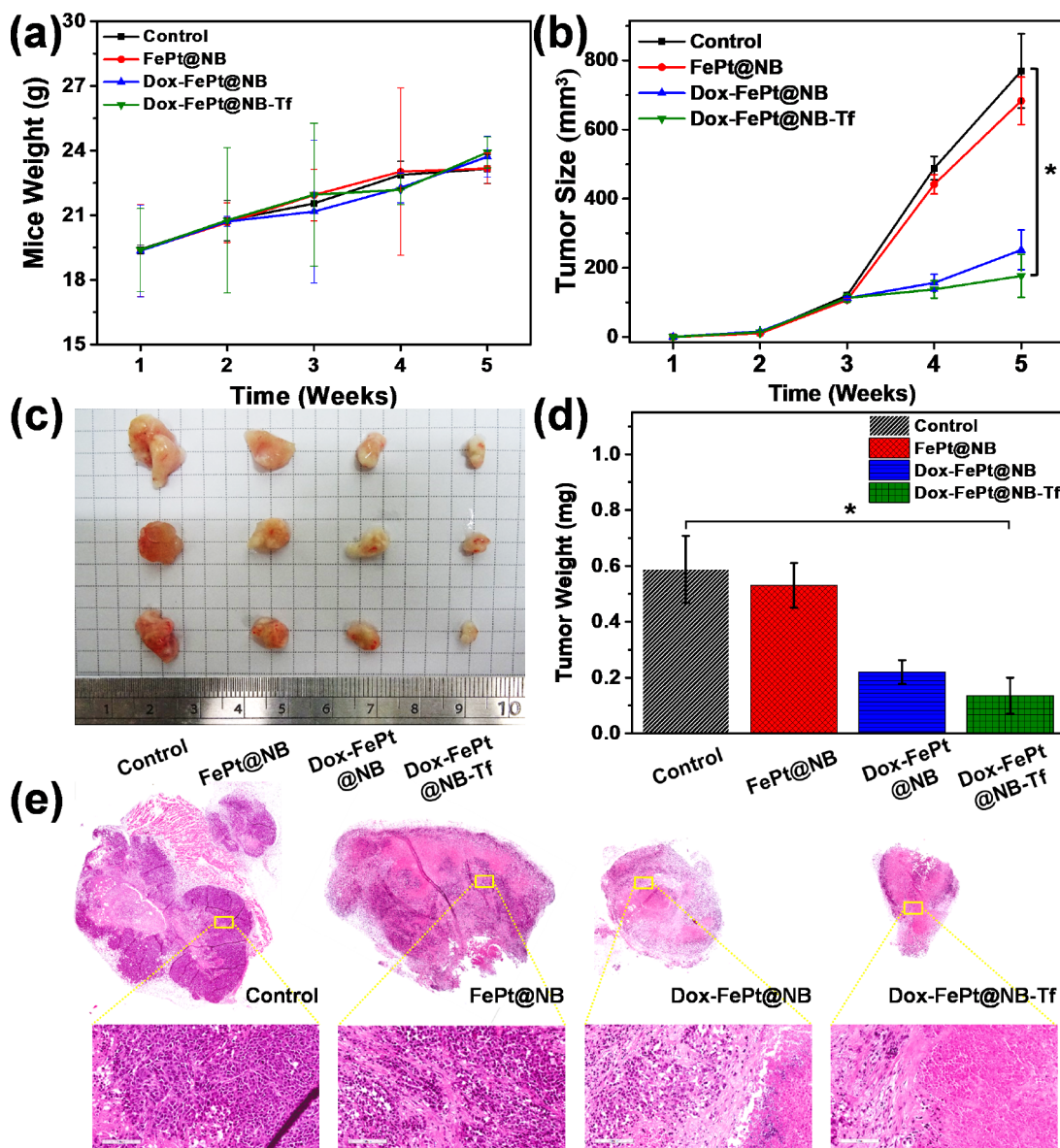


Figure 5. *In vivo* I.V. injection for the treatment of GBM tumors. (a) The weights of the mice were monitored for 5 weeks. The weight of the mice increased from 19 to 24 g. (b) Volumes of tumors from the control, FePt@NB, Dox-FePt@NB, and Dox-FePt@NB-Tf groups. $n = 6$ per group ($*p < 0.05$ compared to the control group). (c) Comparisons of the true tumor sizes of the control, FePt@NB, Dox-FePt@NB, and Dox-FePt@NB-Tf groups. (d) Weights of tumors from the control, FePt@NB, Dox-FePt@NB, and Dox-FePt@NB-Tf groups. (e) Groups with the collected tumor tissue and H&E staining. The full tumor images were obtained at a 5 \times visual magnification level, and the close-up images of the tumor reveal that the detailed tumor cell conditions were obtained at a 40 \times magnification level (scale bar: 200 nm).

compared to FePt@NB or Dox-FePt@NB. We injected nanomaterials intravenously into NS mice and treated them with ultrasound at three different time points (days 21, 25, and 29) after they had been implanted with D54MG subcutaneously and orthotopic brain tumors and tracked their tumor progression regularly. We sacrificed the mice on the 35th day and collected their tumors for analysis (Figure 5a). The size of the tumor decreased significantly with both Dox-FePt@NB and Dox-FePt@NB-Tf treatment, but an even larger decrease was observed with Dox-FePt@NB-Tf treatment (Figure 5b). Compared with the control group, Dox-FePt@NB-Tf treatment almost completely suspended tumor growth and even reduced the tumor size by almost 70% after 5 weeks of cultivation. Even with Dox-FePt@NB treatment, the tumor size was reduced by approximately 60% in contrast to the

control group because of the passive accumulation effect of the nanobubbles (Figure 5c,d).

To explore the results of animal experiments, we used Ki67 (anti-Ki67 antibody, Abcam, ab92742) and cleaved caspase-3 (cleaved caspase-3 antibody, Cell Signaling, #9661) immunohistochemically staining to try to evaluate the proliferation and apoptosis of cells in the tissue. In Figure S10a, Ki67 staining demonstrates the staining intensity and amounts are fewer in the Dox-FePt@NB-Tf group than other treatment groups but the cleaved caspase-3 has been stained in the parts marked with red arrows. The statistical results of staining demonstrated in Figure S10b may indicate that the Dox-FePt@NB-Tf can target more specifically than the Dox-FePt@NB particles to the tumor tissue to affect their ability of proliferation and induce apoptotic pathways to make cell death. In Figure S10c,d, we

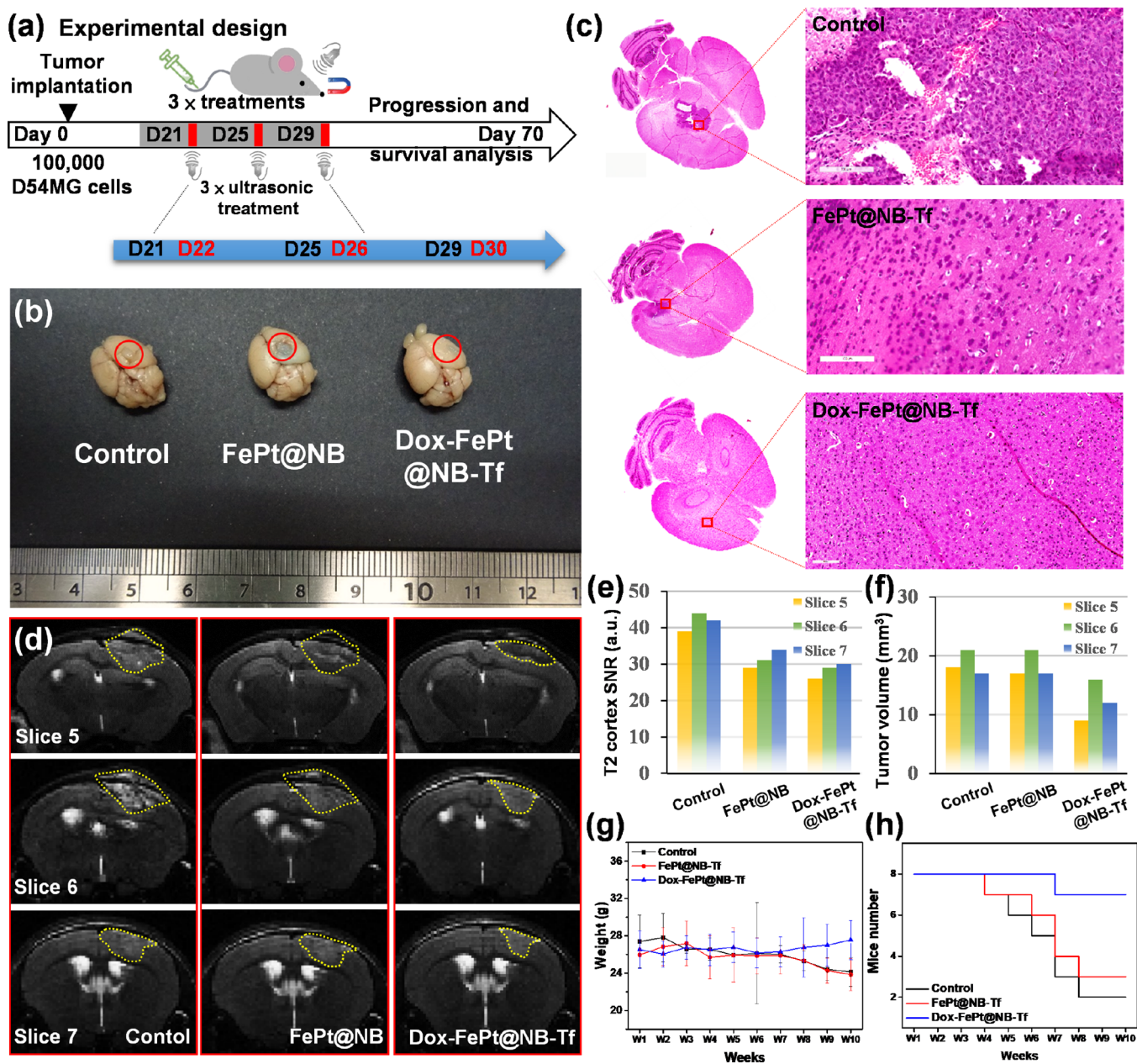


Figure 6. Orthotopic GBM therapeutic and diagnostic evaluation. (a) Mouse examination plan showing the I.V. drug administration for GBM treatment. On the first treatment day, the Dox-FePt@NB-Tf material was injected into the mouse through a tail vein, and strong magnets were used to help the nanocomposite accumulate in the tumor area. On the second treatment day, ultrasonic waves were used to break the NBs and release Dox into the brain tissue. (b) Photos of mouse brains with GBM tumors. The tumors are circled in all three treatment groups: control, FePt@NB, and Dox-FePt@NB-Tf. (c) Brain tissues with H&E staining of the mice from the three treatment groups. The images of the full brain were obtained at a visual magnification of 5X, and the detailed images of the tumor revealed that the tumor cell conditions were obtained at visual magnifications of 40X (scale bar: 200 nm). (d) T2-weighted MRI images of mouse brains with GBMs. The GBM tumors are highlighted in yellow. The quantification values are based on MRI results of the (e) T2 cortex SNR and (f) tumor volume. (g) Weight and (h) survival curves of orthotopic GBM therapeutic mice ($n = 8$).

added an extra Dox-only test group to compare with the Dox-FePt@NB and Dox-FePt@NB-Tf groups. It can be observed that the inhibitory effect of Dox on tumors is less significant than those of Dox-FePt@NB and Dox-FePt@NB-Tf groups. Because all of the *in vivo* experimental groups use a magnetic field under MRI analysis (Figure 3a), this result might indicate that the Dox-FePt@NB has the effect of actively accumulating cancer cells through the application of a magnetic field to induce the material to accumulate cancer cells, resulting in the insignificant difference between the Dox-FePt@NB and Dox-

FePt@NB-Tf groups. Based on recent literature reports, the liver and other tissues may absorb FePt NPs and cause the cumulative effect not to be significant. Conjugate specific tumor-targeting ligands such as Tf can enhance the targeting effect of magnetic nanoparticles. It can shorten the stagnation time of the drug carrier in the blood and that the induction of an external magnetic field and Tf molecular targeting can both increase the accumulation of the material in cancer cells.^{46–48} Next, the glioma-specific therapeutic effect was confirmed by H&E staining, confirming that the tumor tissues had been

damaged by Dox-FePt@NB and Dox-FePt@NB-Tf treatments (Figure 5e). These results indicated that Dox-FePt@NB-Tf had superior therapeutic efficacy to reduce disease progression *in vivo*.

Therapeutic Effects and Image Tracking Abilities of Dox-FePt@NB-Tf *In Situ*. To confirm the therapeutic effect and image tracking abilities of Dox-FePt@NB-Tf *in situ*, we examined NS mice bearing D54MG brain orthotopic tumor implantation treated with ultrasonic materials via intravenous injection three times, on progression days 21, 25, and 29 (Figure 6a). The brain organs were then collected for therapeutic analyses (Figure 6b). To determine that FePt NPs can enter the intracranial tissue through HIFU treatment, the ultrasonic cavitation effect induced the BBB to open temporarily, as shown in Figure S11a. Because GBM can self-regenerate blood vessels, the accumulation of materials by normal intracranial tissues is more clearly observed. After treatment with 7 MHz HIFU, FePt NPs accumulated on the surface of the brain. Regarding GBM orthotopic theranostics, we first confirmed the therapeutic effect of gliomas via histological examination with H&E staining and confirmed that the brain tissues recovered with Dox-FePt@NB and Dox-FePt@NB-Tf treatment (Figure 6c). Next, we monitored the Dox-FePt@NB-Tf performance in the mouse brain and observed that FePt could be applied for T2-weighted MRI. T2-weighted time course detection has been added to Figure S11b. After injecting the material by intravenous injection and the accumulation for 5 and 10 min, the contrast situation where the brain tumor area is darkened can be observed. We also use high-resolution MRI to show the long-term changes in the intensity of FePt, and the size of the tumor was reduced after intravenous injection of Dox-FePt@NB-Tf for 3 weeks, indicating that the accumulation of nanocomposites in the brain needed time to arrive at the tumor site (Figure 6d). We considered that NBs with ultrasound treatment that generated transient cavitation would release the tight junctions of the BBB, which could be examined at the circular point of the brain and send FePt in GBM cells. To evaluate GBM growth inhibition, we quantified the MRI results to confirm the changes in the mouse brain for 3 weeks. In Figure 6e,f, three different groups were used to treat the GBM cells: control, FePt@NB, and Dox-FePt@NB-Tf. Figure 6d shows that the size of the GBM decreased in the Dox-FePt@NB-Tf group. Moreover, T2-weighted MRI indicated that the GBM cells became darker after FePt accumulation. Additionally, the ICP-MS data were evaluated to confirm the targeting capability of Tf and the efficacy of ultrasonic treatment. The survival curve analysis has been added to Figure 6h. We will sacrifice all mice after 10 weeks ($n = 8$). The weight evaluation is also added to Figure 6g to confirm the changes of the different treatment groups. Meanwhile, the material distribution of the entire mouse body was evaluated at the same time to confirm that Dox-FePt@NB-Tf can indeed enter the mouse glioma for accumulation and treatment. First, the PKH26 red fluorescent lipid layer linker was used to label the accumulation of FePt@NBs in different tissues (Figure S12). To avoid autofluorescence and tissue shielding in mice, mouse organs were taken out for the measurement by the fluorescence signal, which was evaluated under the conditions of $\lambda_{\text{ex}} = 535 \text{ nm}$; $\lambda_{\text{em}} = 580 \text{ nm}$ under IVIS detection. In the control group directly injected into PKH26, almost no fluorescence signal is accumulated in the brain. The FePt@NB and FePt@NB-Tf group have the accumulation of the brain tissue. Based on the

IVIS results, the FePt@NB-Tf group has a more obvious accumulation effect. According to the results obtained from the inductively coupled plasma mass spectrometry (ICP-MS) data, due to the targeted guidance of FePt@NB-Tf, the total amount of FePt nanoparticles accumulated in the brain was significantly improved (Figure S13). The total amount of FePt in other organs (e.g., spleen, liver, and kidney) was also increased partly due to the addition of FePt@NB. Notably, because the material was fed via IV, FePt@NB in the blood could reach the brain because of Tf-targeted accumulation, thereby reducing the content in the blood. Thus, the design of Dox-FePt@NB-Tf can allow drugs to accumulate in GBM to improve the effectiveness of treatment and diagnosis.

CONCLUSIONS

Nanobubble cavitation bioimaging displays the mean intensity of acoustic cavitation over time and is correlated with areas of acoustic cavitation-induced BBB opening. At present, there are still not many articles using nanomaterials to actively pass through the blood–brain barrier and perform MRI detection of glioblastoma. This research work provides a nanoplatform combining ultrasonic and specific targeting technology together and enhances the accumulation of magnetic nanomaterial FePt in glioblastoma. After the FePt NPs are encapsulated in the lipid bubbles, the nanocomposite enhances ultrasonic and optical imaging and optimizes the conditions of the T2-weighted MRI signals to improve the detection of the brain tumor. Those results demonstrate that this is an impressive way to accumulate magnetic materials through the BBB. We integrate these technologies for the first time and research early theranostics of glioblastoma. The MRI images from our experiments confirmed that the FePt@NBs successfully guided the hydrophobic chemotherapeutic Dox drug to GBM, where HIFU oscillation broke the NBs to generate a transient cavitation opening in the BBB, allowing the drugs to bypass it and enter the brain to treat the GBM tumor.

ASSOCIATED CONTENT

Supporting Information

The Supporting Information is available free of charge at <https://pubs.acs.org/doi/10.1021/acsami.1c04990>.

Experimental procedures, TEM, DLS, MRI, and MS results being measured further to check the composition of FePt nanoparticles and NBs, *in silico* data and immunostaining results being evaluated with the expression of TfR, and the IVIS and ICP-MS results being supplied as biodistribution detecting methods (PDF)

AUTHOR INFORMATION

Corresponding Authors

Ru-Shi Liu – Department of Chemistry, National Taiwan University, Taipei 10617, Taiwan; orcid.org/0000-0002-1291-9052; Email: rslu@ntu.edu.tw

Michael Hsiao – Genomics Research Center, Academia Sinica, Taipei 11529, Taiwan; Kaohsiung Medical University, Kaohsiung 80708, Taiwan; orcid.org/0000-0001-8529-9213; Email: mhsiao@gate.sinica.edu.tw

Authors

Ming-Hsien Chan – Genomics Research Center, Academia Sinica, Taipei 11529, Taiwan

William Chen – Upper School, Taipei American School, Taipei 11152, Taiwan

Chien-Hsiu Li – Genomics Research Center, Academia Sinica, Taipei 11529, Taiwan

Chih-Yeu Fang – Genomics Research Center, Academia Sinica, Taipei 11529, Taiwan

Yu-Chan Chang – Department of Biomedical Imaging and Radiological Sciences, National Yang Ming Chiao Tung University, Taipei 11221, Taiwan

Da-Hua Wei – Graduate Institute of Manufacturing Technology and Department of Mechanical Engineering, National Taipei University of Technology, Taipei 10608, Taiwan; orcid.org/0000-0001-7603-3739

Complete contact information is available at:

<https://pubs.acs.org/10.1021/acsami.1c04990>

Author Contributions

[○]M.-H.C. and W.C. contributed equally as co-first authors.

Notes

The authors declare no competing financial interest.

ACKNOWLEDGMENTS

This research was supported by the Ministry of Science and Technology [MOST 109-2113-M-002-020-MY3 and MOST 107-2113-M-002-008-MY3] to R.S.L. and [MOST 110-2731-M-027-001 and MOST 108-2628-E-027-002-MY3] to D.H.W. The authors would like to express their gratitude to Ms. Chia-Ying Chien of the Ministry of Science and Technology (National Taiwan University) for assistance in the TEM experiment. The authors would also like to thank Ms. L.W. Lo and Ms. H.F. Tsai of the Genomics Research Center, Academia Sinica, for help with confocal microscopy, H&E, and immunostaining.

REFERENCES

- (1) Kinoshita, M.; McDannold, N.; Jolesz, F. A.; Hynynen, K. Noninvasive Localized Delivery of Herceptin to the Mouse Brain by MRI-Guided Focused Ultrasound-Induced Blood-Brain Barrier Disruption. *Proc. Natl. Acad. Sci.* **2006**, *103*, 11719–11723.
- (2) Lakkadwala, S.; dos Santos Rodrigues, B.; Sun, C.; Singh, J. Dual Functionalized Liposomes for Efficient Co-Delivery of Anti-Cancer Chemotherapeutics for the Treatment of Glioblastoma. *J. Controlled Release* **2019**, *307*, 247–260.
- (3) Zhao, P.; Le, Z.; Liu, L.; Chen, Y. Therapeutic Delivery to the Brain via the Lymphatic Vasculature. *Nano Lett.* **2020**, *20*, 5415–5420.
- (4) Zhao, M.; Bozzato, E.; Joudiou, N.; Ghiassinejad, S.; Danhier, F.; Gallez, B.; Pr at, V. Codelivery of Paclitaxel and Temozolomide through a Photopolymerizable Hydrogel Prevents Glioblastoma Recurrence after Surgical Resection. *J. Controlled Release* **2019**, *309*, 72–81.
- (5) Kong, X. T.; Nguyen, N. T.; Choi, Y. J.; Lassman, A. B. Phase 2 Study of Bortezomib Combined With Temozolomide and Regional Radiation Therapy for Upfront Treatment of Patients With Newly Diagnosed Glioblastoma Multiforme: Safety and Efficacy Assessment. *Int. J. Radiat. Oncol.* **2019**, *103*, 1289–1289.
- (6) Yusuf, M. B.; Gaskins, J.; Amsbaugh, M. J.; Woo, S.; Burton, E. Survival Impact of Prolonged Postoperative Radiation Therapy for Patients with Glioblastoma Treated with Combined-Modality Therapy. *Neuro-Oncol. Pract.* **2019**, *6*, 112–123.
- (7) Zobel, K.; Hansen, U.; Galla, H. J. Blood-Brain Barrier Properties in Vitro Depend on Composition and Assembly of Endogenous Extracellular Matrices. *Cell Tissue Res.* **2016**, *365*, 233–245.
- (8) Gaudin, A.; Tagit, O.; Sobot, D.; Lepetre-Mouelhi, S.; Mougin, J.; Martens, T. F.; Braeckmans, K.; Nicolas, V.; Desma le, D.; de Smedt, S. C.; Hildebrandt, N.; Couvreur, P.; Andrieux, K. Transport Mechanisms of Squalenoyl-Adenosine Nanoparticles Across the Blood-Brain Barrier. *Chem. Mater.* **2015**, *27*, 3636–3647.
- (9) Bukchin, A.; Sanchez-Navarro, M.; Carrera, A.; Teixid , M.; Carcaboso, A. M.; Giralt, E.; Sosnik, A. Amphiphilic Polymeric Nanoparticles Modified with a Retro-Enantio Peptide Shuttle Target the Brain of Mice. *Chem. Mater.* **2020**, *32*, 7679–7693.
- (10) Porret, E.; Sancey, L.; Mart n-Serrano, A.; Mont n z, M. I.; Seeman, R.; Yahia-Arnmar, A.; Okuno, H.; Gomez, F.; Ariza, A.; Hildebrandt, N.; Fleury, J.-B.; Coll, J.-L.; Le G uevel, X. Hydrophobicity of Gold Nanoclusters Influences Their Interactions with Biological Barriers. *Chem. Mater.* **2017**, *29*, 7497–7506.
- (11) Hynynen, K.; McDannold, N.; Vykhodtseva, N.; Raymond, S.; Weissleder, R.; Jolesz, F. A.; Sheikov, N. Focal Disruption of the Blood-Brain Barrier due to 260-kHz Ultrasound Bursts: a Method for Molecular Imaging and Targeted Drug Delivery. *J. Neurosurg.* **2006**, *105*, 445–454.
- (12) Carpentier, A.; Canney, M.; Vignot, A.; Reina, V.; Beccaria, K.; Horodyckid, C.; Karachi, C.; Leclercq, D.; Lafon, C.; Chapelon, J. Y.; Capelle, L.; Cornu, P.; Sanson, M.; Hoang-Xuan, K.; Delattre, J. Y.; Idhah, A. Clinical Trial of Blood-Brain Barrier Disruption by Pulsed Ultrasound. *Sci. Transl. Med.* **2016**, *8*, 343re2.
- (13) Liu, C.; Chen, J.; Zhu, Y.; Gong, X.; Zheng, R.; Chen, N.; Chen, D.; Yan, H.; Zhang, P.; Zheng, H.; Sheng, Z.; Song, L. Highly Sensitive MoS₂-Indocyanine Green Hybrid for Photoacoustic Imaging of Orthotopic Brain Glioma at Deep Site. *Nanomicro. Lett.* **2018**, *10* No. 48.
- (14) Beccaria, K.; Canney, N.; Bouchoux, G.; Zohar, S.; Boddaert, N.; Bourdeaut, F.; Doz, F.; Dufour, C.; Grill, J.; Carpentier, A.; Puget, S. Safety of Ultrasound-Induced Blood-Brain Barrier Opening in Pediatric Patients with Refractory Sus-Tentorial Malignant Brain Tumors before Chemotherapy Administration - the Sonokid Clinical Trial. *Neuro-Oncology* **2018**, *20*, 146–146.
- (15) Bing, C.; Hong, Y.; Hernandez, C.; Rich, M.; Cheng, B.; Munaweera, I.; Szczepanski, D.; Xi, Y.; Bolding, M.; Exner, A.; Chopra, R. Characterization of Different Bubble Formulations for Blood-Brain Barrier Opening Using a Focused Ultrasound System with Acoustic Feedback Control. *Sci. Rep.* **2018**, *8*, 7986.
- (16) Idhah, A.; Canney, M.; Vignot, A.; Law-Ye, B.; Dehais, C.; Houillier, C.; Laigle-Donadey, F.; Delattre, J. Y.; Carpentier, A. Phase I/II Study of an Implantable Device Delivering Low Intensity Pulsed Ultrasound (LIPU) to Disrupt the Blood-Brain Barrier (BBB) Followed by Intravenous Carboplatin Chemotherapy in Patients with Recurrent Glioblastoma (GBM). *J. Clin. Oncol.* **2017**, *35*, 2034–2034.
- (17) Sarkaria, J. N.; Hu, L. S.; Parney, I. F.; Pafundi, D. H.; Brinkmann, D. H.; Laack, N. N.; Giannini, C.; Burns, T. C.; Kizilbash, S. H.; Laramy, J. K.; Swanson, K. R.; Kaufmann, T. J.; Brown, P. D.; Agar, N. Y. R.; Galanis, E.; Buckner, J. C.; Elmquist, W. F. Is the Blood-Brain Barrier Really Disrupted in All Glioblastomas? A Critical Assessment of Existing Clinical Data. *Neuro-Oncology* **2018**, *20*, 184–191.
- (18) Dubois, L. G.; Campanati, L.; Righy, C.; D'Andrea-Meira, I.; Spohr, T. C. L. D. E.; Porto-Carreiro, I.; Pereira, C. M.; Balca-Silva, J.; Kahn, S. A.; DosSantos, M. F.; Oliveira, M. D. R.; Ximenes-da-Silva, A.; Lopes, M. C.; Faveret, E.; Gasparetto, E. L.; Moura-Neto, V. Gliomas and the Vascular Fragility of the Blood Brain Barrier. *Front. Cell Neurosci.* **2014**, *8*, 418.
- (19) Arvanitis, C. D.; Ferraro, G. B.; Jain, R. K. The Blood-Brain Barrier and Blood-Tumour Barrier in Brain Tumours and Metastases. *Nat. Rev. Cancer* **2020**, *20*, 26–41.
- (20) Luo, Z.; Jin, K.; Pang, Q.; Shen, S.; Yan, Z.; Jiang, T.; Zhu, X.; Yu, L.; Pang, Z.; Jiang, X. On-Demand Drug Release from Dual-Targeting Small Nanoparticles Triggered by High-Intensity Focused

Ultrasound Enhanced Glioblastoma-Targeting Therapy. *ACS Appl. Mater. Interfaces* **2017**, *9*, 31612–31625.

(21) Idbaih, A.; Canney, M.; Belin, L.; Desseaux, C.; Vignot, A.; Bouchoux, G.; Asquier, N.; Law-Ye, B.; Leclercq, D.; Bissery, A.; De Rycke, Y.; Trosch, C.; Capelle, L.; Sanson, M.; Hoang-Xuan, K.; Dehais, C.; Houillier, C.; Laigle-Donadey, F.; Mathon, B.; André, A.; Lafon, C.; Chapelon, J. Y.; Delattre, J. Y.; Carpentier, A. Safety and Feasibility of Repeated and Transient Blood-Brain Barrier Disruption by Pulsed Ultrasound in Patients with Recurrent Glioblastoma. *Clin. Cancer Res.* **2019**, *25*, 3793–3801.

(22) Pellow, C.; O'Reilly, M. A.; Hynynen, K.; Zheng, G.; Goertz, D. E. Simultaneous Intravital Optical and Acoustic Monitoring of Ultrasound-Triggered Nanobubble Generation and Extravasation. *Nano Lett.* **2020**, *20*, 4512–4519.

(23) Huang, H. Y.; Liu, H. L.; Hsu, P. H.; Chiang, C. S.; Tsai, C. H.; Chi, H. S.; Chen, S. Y.; Chen, Y. Y. A Multitheragnostic Nanobubble System to Induce Blood-Brain Barrier Disruption with Magnetically Guided Focused Ultrasound. *Adv. Mater.* **2015**, *27*, 655–661.

(24) Burgess, A.; Hynynen, K. Noninvasive and Targeted Drug Delivery to the Brain Using Focused Ultrasound. *ACS Chem. Neurosci.* **2013**, *4*, 519–526.

(25) Fu, W.; You, C.; Ma, L.; Li, H.; Ju, Y.; Guo, X.; Shi, S.; Zhang, T.; Zhou, R.; Lin, Y. Enhanced Efficacy of Temozolomide Loaded by a Tetrahedral Framework DNA Nanoparticle in the Therapy for Glioblastoma. *ACS Appl. Mater. Interfaces* **2019**, *11*, 39525–39533.

(26) Luo, M.; Lewik, G.; Ratcliffe, J. C.; Choi, C. H. J.; Mäkilä, E.; Tong, W. Y.; Voelcker, N. H. Systematic Evaluation of Transferrin-Modified Porous Silicon Nanoparticles for Targeted Delivery of Doxorubicin to Glioblastoma. *ACS Appl. Mater. Interfaces* **2019**, *11*, 33637–33649.

(27) Jhaveri, A.; Deshpande, P.; Pattni, B.; Torchilin, V. Transferrin-Targeted, Resveratrol-Loaded Liposomes for the Treatment of Glioblastoma. *J. Controlled Release* **2018**, *277*, 89–101.

(28) Salzano, G.; Zappavigna, S.; Luce, A.; D'Onofrio, N.; Balestrieri, M. L.; Grimaldi, A.; Lusa, S.; Ingrosso, D.; Artuso, S.; Porru, M.; Leonetti, C.; Caraglia, M.; De Rosa, G. Transferrin-Targeted Nanoparticles Containing Zoledronic Acid as a Potential Tool to Inhibit Glioblastoma Growth. *J. Biomed. Nanotechnol.* **2016**, *12*, 811–830.

(29) Lam, F. C.; Morton, S. W.; Wyckoff, J.; Han, T.-L. V.; Hwang, M. K.; Maffa, A.; Balkanska-Sinclair, E.; Yaffe, M. B.; Floyd, S. R.; Hammond, P. T. Enhanced Efficacy of Combined Temozolomide and Bromodomain Inhibitor Therapy for Gliomas Using Targeted Nanoparticles. *Nat. Commun.* **2018**, *9*, 1991.

(30) Pandey, A.; Singh, K.; Patel, S.; Singh, R.; Patel, K.; Sawant, K. Hyaluronic Acid Tethered pH-Responsive Alloy-Drug Nanoconjugates for Multimodal Therapy of Glioblastoma: An Intranasal Route Approach. *Mat. Sci. Eng. C* **2019**, *98*, 419–436.

(31) Franchini, R.; Casciaro, E.; Conversano, F.; Lay-Ekuakille, A.; Casciaro, S. Simulated Measurements of the Magnetic Behavior of New Dual-Mode Nanosized Contrast Agents. *Ieee Trans. Nanotechnol.* **2017**, *16*, 842–850.

(32) Chou, S. W.; Shau, Y. H.; Wu, P. C.; Yang, Y. S.; Shieh, D. B.; Chen, C. C. In Vitro and in Vivo Studies of FePt Nanoparticles for Dual Modal CT/MRI Molecular Imaging. *J. Am. Chem. Soc.* **2010**, *132*, 13270–13278.

(33) Pan, Y.; Du, X.; Zhao, F.; Xu, B. Magnetic Nanoparticles for the Manipulation of Proteins and Cells. *Chem. Soc. Rev.* **2012**, *41*, 2912–2942.

(34) Ni, D.; Zhang, J.; Bu, W.; Xing, H.; Han, F.; Xiao, Q.; Yao, Z.; Chen, F.; He, Q.; Liu, J.; Zhang, S.; Fan, W.; Zhou, L.; Peng, W.; Shi, J. Dual-Targeting Upconversion Nanoprobes Across the Blood-Brain Barrier for Magnetic Resonance/Fluorescence Imaging of Intracranial Glioblastoma. *ACS Nano* **2014**, *8*, 1231–1242.

(35) Liang, K.; Li, Z.; Luo, Y.; Zhang, Q.; Yin, F.; Xu, L.; Chen, H.; Wang, H. Intelligent Nanocomposites with Intrinsic Blood-Brain-Barrier Crossing Ability Designed for Highly Specific MR Imaging and Sonodynamic Therapy of Glioblastoma. *Small* **2020**, *16*, No. e1906985.

(36) Li, B.; Xiao, H.; Cai, M.; Li, X.; Xu, X.; Wang, S.; Huang, S.; Wang, Y.; Cheng, D.; Pang, P.; Shan, H.; Shuai, X. Molecular Probe Crossing Blood–Brain Barrier for Bimodal Imaging–Guided Photo-thermal/Photodynamic Therapies of Intracranial Glioblastoma. *Adv. Funct. Mater.* **2020**, *30*, 1909117.

(37) Kalidasan, V.; Liu, X. L.; Heng, T. S.; Yang, Y.; Ding, J. Bovine Serum Albumin-Conjugated Ferrimagnetic Iron Oxide Nanoparticles to Enhance the Biocompatibility and Magnetic Hyperthermia Performance. *Nanomicro Lett.* **2016**, *8*, 80–93.

(38) Saraiva, C.; Praça, C.; Ferreira, R.; Santos, T.; Ferreira, L.; Bernardino, L. Nanoparticle-Mediated Brain Drug Delivery: Overcoming Blood-Brain Barrier to Treat Neurodegenerative Diseases. *J. Controlled Release* **2016**, *235*, 34–47.

(39) Niu, X.; Chen, J.; Gao, J. Nanocarriers as a Powerful Vehicle to Overcome Blood-Brain Barrier in Treating Neurodegenerative Diseases: Focus on Recent Advances. *Asian J. Pharm. Sci.* **2019**, *14*, 480–496.

(40) Hanson, L. R.; Frey, W. H., II Intranasal Delivery Bypasses the Blood-Brain Barrier to Target Therapeutic Agents to the Central Nervous System and Treat Neurodegenerative Disease. *BMC Neurosci.* **2008**, *9*, No. S5.

(41) Chou, S. W.; Liu, C. L.; Liu, T. M.; Shen, Y. F.; Kuo, L. C.; Wu, C. H.; Hsieh, T. Y.; Wu, P. C.; Tsai, M. R.; Yang, C. C.; Chang, K. Y.; Lu, M. H.; Li, P. C.; Chen, S. P.; Wang, Y. H.; Lu, C. W.; Chen, Y. A.; Huang, C. C.; Wang, C. R. C.; Hsiao, J. K.; Li, M. L.; Chou, P. T. Infrared-Active Quadruple Contrast FePt Nanoparticles for Multiple Scale Molecular Imaging. *Biomaterials* **2016**, *85*, 54–64.

(42) Kang, E.; Jung, H.; Park, J. G.; Kwon, S.; Shim, J.; Sai, H.; Wiesner, U.; Kim, J. K.; Lee, J. Block Copolymer Directed One-Pot Simple Synthesis of L1₀-Phase FePt Nanoparticles inside Ordered Mesoporous Aluminosilicate/Carbon Composites. *ACS Nano* **2011**, *5*, 1018–1025.

(43) Fan, K.; Jia, X.; Zhou, M.; Wang, K.; Conde, J.; He, J.; Tian, J.; Yan, X. Ferritin Nanocarrier Traverses the Blood Brain Barrier and Kills Glioma. *ACS Nano* **2018**, *12*, 4105–4115.

(44) Liu, R.; Tang, J.; Xu, Y.; Dai, Z. Bioluminescence Imaging of Inflammation in Vivo Based on Bioluminescence and Fluorescence Resonance Energy Transfer Using Nanobubble Ultrasound Contrast Agent. *ACS Nano* **2019**, *13*, 5124–5132.

(45) Nittayacharn, P.; Abenojar, E.; de Leon, A.; Wegierak, D.; Exner, A. A. Increasing Doxorubicin Loading in Lipid-Shelled Perfluoropropane Nanobubbles via a Simple Deprotonation Strategy. *Front. Pharmacol.* **2020**, *11*, 644.

(46) Gallo, J.; Long, N. J.; Aboagye, E. O. Magnetic Nanoparticles as Contrast Agents in the Diagnosis and Treatment of Cancer. *Chem. Soc. Rev.* **2013**, *42*, 7816–7833.

(47) Jiang, X.; Weise, S.; Hafner, M.; Rocker, C.; Zhang, F.; Parak, W. J.; Nienhaus, G. U. Quantitative Analysis of the Protein Corona on FePt Nanoparticles Formed by Transferrin Binding. *J. R. Soc., Interface* **2010**, *7*, S5–S13.

(48) Kresse, M.; Wagner, S.; Pfeifferer, D.; Lawaczek, R.; Elste, V.; Semmler, W. Targeting of Ultrasmall Superparamagnetic Iron Oxide (USPIO) Particles to Tumor Cells in Vivo by Using Transferrin Receptor Pathways. *Magn. Reson. Med.* **1998**, *40*, 236–242.